

CFD estimation of heat losses in thermal conductivity measurements

Wojciech Adamczyk, Filip Szelejewski, Paweł Kozołub,
Ryszard Białeczki, Tadeusz Kruczek
Institute of Thermal Technology, Silesian University of Technology
Konarskiego 22 44-100 Gliwice, Poland
e-mail: wojciech.adamczyk@polsl.pl

Knowledge of a material thermal conductivity is essential in several engineering applications. This material property serves also as a measure of the quality of manufactured materials. Nowadays, a lot of effort is directed into development of non-destructive, fast and reliable measurement techniques. In the works of Adamczyk *et al.* [1] and Kruczek *et al.* [10], a new *in situ* conductivity measurement technique for an anisotropic material was developed. This method, due to its rapidity and nondestructive character, can be embedded in a manufacturing process. However, despite many advantages, the developed measuring technique has some drawbacks corresponding to the applied mathematical model, which is used for determining the material thermal conductivities. It neglects the effect of heat losses due to radiation and convection phenomena on the calculated values of thermal conductivities. In this work, the computational fluid dynamic (CFD) modeling was applied to estimate heat losses due to radiation and convection. The influence of omitting the radiative and convective heat transfer on the predicted temperature field and calculated thermal conductivities was investigated. Evaluated numerical results were compared against experimental data by using the developed *in situ* measurement technique for the thermal conductivity of anisotropic materials.

Keywords: thermal conductivity, in-situ method, CFD, radiation, natural convection.

1. INTRODUCTION

The thermal conductivity assessment is essential in several engineering applications. Simulations of heat conduction in solids, estimation of heat losses, inspection of material's admissible temperature levels, and calculation of thermal stresses are a few examples of industrial cases, where the value of heat conductivity is needed. This material's property is also often used as a measure of the quality of manufactured materials. The production of insulating or carbon materials is a good example of such applications. Specialized laboratories perform the heat conductivity measurements using a commercially available equipment. Nevertheless, in spite of a large number of such sites and variety of measurement methods available, a lot of effort is directed into the development of non-destructive, fast and reliable measurement techniques. Moreover, there is no universal technique which is applicable to all materials and temperature ranges.

The current state of the art for heat diffusivity and conductivity measurements is described in [5] and [7], where the existing methods are discussed in terms of their advantages, disadvantages and fields of application. Nowadays, the Parker flash method [12] is well-known and widely used for determining the thermal diffusivity, heat capacity and thermal conductivity. It is a transient-state technique which main advantage is a short time of measurement. Nevertheless, this method has also disadvantages, namely its destructive character and its 1D model assumption, which in the case of anisotropic (orthotropic) material require additional probes and experiments. Even though the technique was extended to deal with anisotropic medium [9], it still cannot be applied for *in situ*

measurements. Nonetheless, the Parker flash technique is still being improved [3] by accounting for heat losses, nonhomogeneous heat distribution of the laser beam, etc. In order to reduce the time required for the sample preparation and measuring process, a new and non-destructive *in situ* measurement technique was proposed in [10]. The entire time required for the measurement and results evaluation is of the order of a minute. Thus, the technique may be used for *on-line* material property measurements, that are embedded in the manufacturing process. The thermal conductivity is retrieved by processing of the temporal and spatial distribution of the temperature field, which is recorded by a fast infrared (IR) camera. Perturbations of the temperature field are induced by a short laser impulse absorbed within a small surface area of the sample. The characteristic feature of the developed technique is that the laser and the IR camera are located on the same side of the sample, which is different from the configuration in the standard Parker flash method [12]. Such a configuration is known in the literature as the *front face* technique. Detailed information about this measuring approach can be found in [10].

The proposed *in situ* technique can be applied for both, orthotropic and isotropic materials. The laser impulse impinges on the one plane surface of the examined material, which is further referred as the *measurement surface*. The measuring procedure is based on the inverse analysis, where the mathematical model is used to solve a boundary value problem, known as the Green's function [4, 8], for a semi-infinite domain with the Neumann boundary condition. The major disadvantage of the developed *in situ* technique is that it neglects heat losses from the measured surface, which are driven by the thermal radiation and convection phenomena. In the present work, the total amount of heat transferred from the measured surface to the surrounding air was calculated using the ANSYS/Fluent computational fluid dynamics (CFD) software. The influence of heat losses on the calculated temperature field and retrieved thermal conductivities of the anisotropic material was investigated. The experimental data used for the model validation was carried out using the *in situ* measurement procedure.

2. EXPERIMENT

The schematic diagram of the experimental facility used for thermal conductivity measurements is depicted in Fig. 1. The detailed description of the measuring device, control equipment used, and methodology can be found in work of Kruczek *et al.* [10]. An anisotropic sample with known material density (1091 kg/m^3) and heat capacity (900 J/kgK) was selected for tests as a benchmark. The geometry of the manufactured sample has a cubic shape with edge size equal to 25 cm.

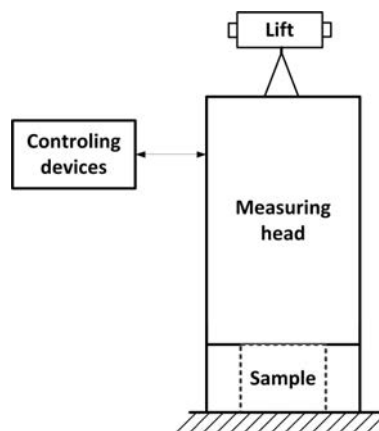


Fig. 1. Schematic diagram of the experimental facility used for measuring thermal conductivities.

Using the *in situ* technique [10], the material thermal conductivity was measured at five randomly selected locations on the external surface of the sample. The measurements were performed

in laboratory conditions, where the ambient temperature was equal to 29°C. In order to even out the differences between sample and ambient temperatures, the sample was exposed to laboratory conditions before the measurement process. Resulting values of thermal conductivities obtained in measurements at five arbitrarily selected points are shown in Table 1. The calculated average value of thermal conductivity in x , y and z direction was equal to 5.15 W/mK, 5.2 W/mK, and 5.2 W/mK, respectively. Retrieved thermal conductivities are kept in the certain range of error, which in the case of the *in situ* technique was calculated as 5% [10].

Table 1. Thermal conductivities measured using *in situ* measurement technique.

Measurement point	λ_x W/mK	$\lambda_y = \lambda_z$ W/mK
1	5.1	5.0
2	4.9	5.2
3	5.4	5.4
4	5.3	5.3
5	5.1	5.1

3. NUMERICAL MODEL

The geometry used for numerical simulations is shown in Fig. 2. The geometry was split into two main zones. The upper zone represents the surrounding air, whereas the bottom zone defines the material. The numerical mesh consist of 930 000 hexahedral elements, with the skewness parameter smaller than 0.05 and element size 0.45 mm. The energy of the laser impulse was simulated using an energy source prescribed to the selected range of the material zone using the user defined function (UDF) tool. The diameter of the laser beam was equal to 1 mm, where the overall laser power was equal to 67.32 W. The laser emission time was set to 0.2 s and it was controlled by the UDF. Figure 2 presents the location where the energy source was prescribed to the model. Due to long calculation time required for the transient simulation, the numerical model of the sample was limited to a quarter with defined symmetry boundary conditions for both air and material zones.

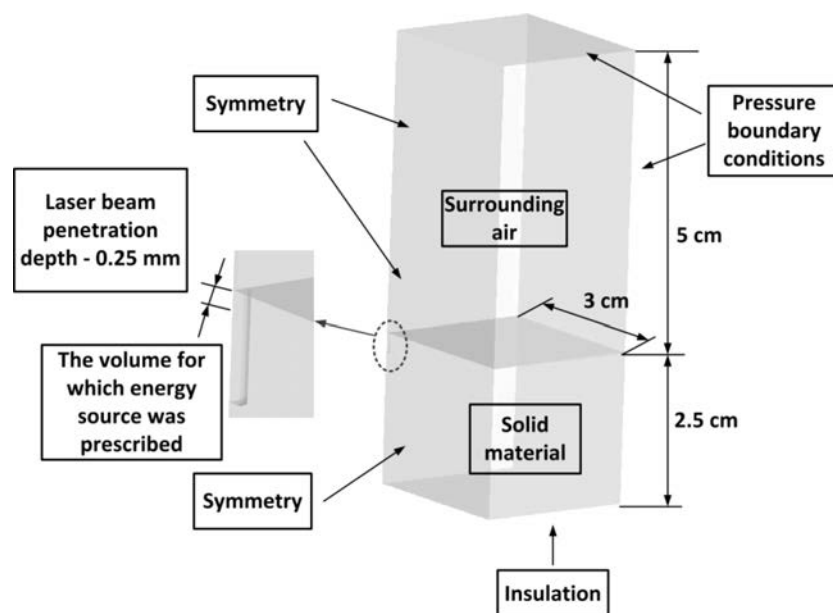


Fig. 2. Numerical model geometry with depicted boundary conditions and characteristic dimensions.

Moreover, its geometrical size was reduced to the range in which the temperature field propagate after the laser emission. During experiments it was observed that after 2 s since the laser energy has been absorbed, the temperature field tends to the initial temperature value. For this time the noticeable changes of the temperature field were observed in the distance of 0.7 cm from the laser emission point. Thus, the computational domain of the sample was limited to $2.5 \times 2.0 \times 2.5$ cm.

Numerical model is based on the solution of the continuity, energy and momentum transport equations. The turbulence was modeled using the $k-\varepsilon$ realizable model with the enhanced wall treatment. The $y+$ parameter for cells adjacent to the surface was smaller than 1, which justified the usage of the advanced models for flow calculations near the wall surface. The radiative heat transfer between walls was modeled using the surface-to-surface (S2S) radiation model implemented as the UDF. Required view factors were calculated using the built-in procedure in the ANSYS Fluent CFD code [2].

The proper buoyancy effect modeling in the natural convection requires additional effort [6]. The body force term in the momentum equation has to be slightly modified in order to take into account buoyancy forces. This modification is included only in the momentum equation and acts in the direction of gravitational acceleration. The modified body force term due to buoyancy takes the form

$$(\rho - \rho_{op})g, \quad (1)$$

where ρ_{op} is the operating density calculated for initial temperature 29°C , g is the gravitational acceleration, ρ is the local density calculated using ideal gas law defined as

$$\rho = \frac{p_{op}M_{gas}}{TR}, \quad (2)$$

where p_{op} is the operating pressure equal to 101.3 kPa, T is the temperature, R defines the universal gas constant (8314.4 J/kmolK), and M_{gas} is the atomic weight equal to 28.966 kg/kmol. For the gravitational acceleration equal to $g_y = -9.81 \text{ m/s}^2$ and local density ρ , which is greater than the operating density ρ_{op} , the fluid is moved upward due to the buoyancy force. During the simulations the density difference at the pressure boundary condition has to be near to zero. This ensures the normal to the boundary wall direction of velocity vectors of the air, which is incoming to the computational domain (reverse flow).

In order to determine the influence of heat losses due to the radiation and convection on the calculated temperature field, a set of numerical simulations was carried out for three model configurations. In *Case A* both, the radiation and convection were included in the numerical model, in *Case B* the radiation was not taken into account, whereas in *Case C* neither the radiation nor convection was considered. The heat losses for *Case A* and *Case B* were calculated during simulations in subsequent time steps. The radiative heat transfer was calculated for an enclosure filled with the medium transparent to the radiation. The enclosure was configured from three surfaces, which are numbered and depicted in Fig. 3. The amount of radiative heat, which was removed from surface 1 and 2, was calculated as

$$Q_{r,1-3} = A_1F_{1-3}(b_1 - b_3), \quad (3)$$

$$Q_{r,2-3} = A_2F_{2-3}(b_2 - b_3), \quad (4)$$

where A is the surface area, F_{1-2} and F_{2-3} are the view factors between surface 1-2 and 2-3, b is the radiosity. Unknown radiosities in Eqs. (3) and (4) were calculated using the radiosity balance formulated as the set of equations defined as

$$A_1b_1 = A_1\varepsilon_1\sigma T_1^4 + (1 - \varepsilon_1)A_3F_{3-1}b_3, \quad (5)$$

$$A_2b_2 = A_2\varepsilon_2\sigma T_2^4 + (1 - \varepsilon_2)A_3F_{3-2}b_3, \quad (6)$$

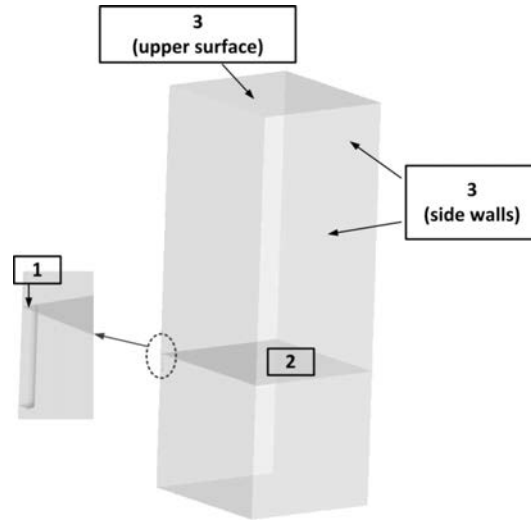


Fig. 3. Surface configuration used for the heat losses calculation due to the thermal radiation.

$$A_3 b_3 = A_3 \varepsilon_3 \sigma T_3^4 + (1 - \varepsilon_3)[A_1 F_{1-3} b_1 + A_2 F_{2-3} b_2], \quad (7)$$

where ε is the surface emissivity and σ stands for the Stefan-Boltzmann constant.

During simulations the ratio of Grashof and Reynolds numbers, defined as Gr/Re^2 , was greater than 16. This indicates that inertia forces were negligible and the flow was dominated by the natural convection. The convective heat transfer for both *Case A* and *Case B* can be calculated as

$$Q_{con} = A_i \alpha \Delta T_i, \quad (8)$$

where subscripts i assume value 1 and 2 for two flat surfaces (see Fig. 3), ΔT is the difference between the surfaces temperature T_i and the temperature of surrounding air T_∞ . The heat transfer coefficient, denoted by α , is defined as

$$\alpha = \frac{\text{Nu} \lambda_f}{l_0}, \quad (9)$$

where Nu is the Nusselt number, λ_f is the thermal conductivity calculated for the air film temperature $T_f = (T_i + T_\infty)/2$, and l_0 is the characteristic dimension which is given by the relation

$$l_0 = \frac{A_i}{U_i}, \quad (10)$$

where A_i and U_i stands for the area and perimeter of the i -th surface, respectively. The Nusselt number in Eq. (9) was calculated using the empirical correlation in the function of the Rayleigh number (Ra), which is defined as the product of the Grashof (Gr) and Prandtl (Pr) numbers, valid in the range from 10^4 to 10^7 [1]

$$\text{Nu} = 0.54 \text{ Ra}^{0.25}. \quad (11)$$

The Grashof number which defines the ratio of buoyancy forces and viscous forces acting on the fluid is defined as

$$\text{Gr} = \frac{g \beta l_0^3 \rho_f^2 \Delta T}{\mu_f^2}, \quad (12)$$

where ρ_f is the density calculated for the film temperature T_f , β is the thermal expansion coefficient defined as $1/T_f$, and μ_f is the dynamic viscosity.

4. NUMERICAL RESULTS

Figure 4 illustrates the calculated heat losses obtained during simulations applying the set of UDFs for *Case A* and *Case B*. The overall heat losses from the measured surface for both *Case A* and *Case B* were calculated using the square integration procedure which calculates the field under evaluated curves, as it is shown in Fig. 4. The integration procedure is given by the following formula:

$$Q = \int_{\tau_0}^{\tau_k} Q(\tau) d\tau = \sum_{i=1}^{N-1} \frac{Q_i + Q_{i+1}}{2} \Delta h, \quad (13)$$

where N is the number of integration points (29), τ_0 is the initial time (0.025 s), τ_k is the final integration time (0.725 s), and Δh is the integration step defined as $(\tau_k - \tau_0)/N$ (0.0241). The calculated heat losses were equal to 2.2 W and 1.7 W for *Case A* and *Case B*, respectively.

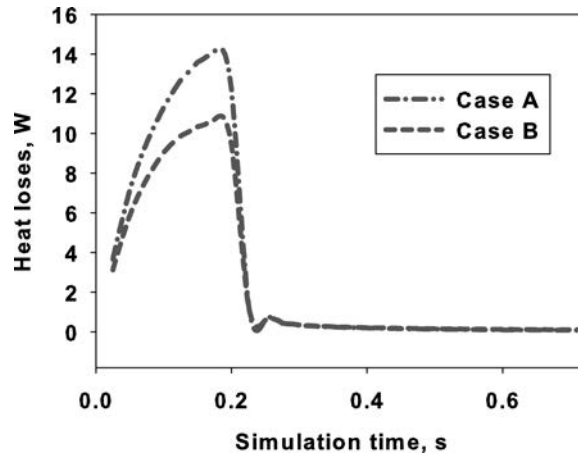


Fig. 4. The changes of heat losses during simulations for *Case A* and *Case B*.

To determine the influence of omitting the radiative and convective heat losses to the temperature field, the position of the selected isotherm (33.1°C) was compared for the measured and calculated temperature field after 0.63 s. Temperature fields acquired using the IR camera consist of temporal and spatial variation of temperature values. The recorded temperature field was limited to the range of 100×100 pixels in order to decrease the calculation time. Each pixel registers the intensity leaving a small square located on the measured surface. These intensities were next transformed to temperature values, which were assigned to centers of the mentioned squares. In the first step of the calculation procedure, the location of the isotherm was determined by the bilinear interpolation performed at four of recorded pixels, as it is illustrated in Fig. 5. As a result of this

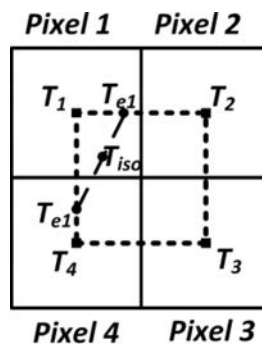


Fig. 5. Bilinear interpolation used for determining the isotherm coordinates.

procedure, a set of points corresponding to the selected value of the isotherm was obtained. Figure 6 shows an exemplary set of such points for a quarter of the temperature field. The square points correspond to pixel locations where temperatures bracketing the isotherm are recorded, whereas the diamond points represent locations determined by the isotherm. The same calculation procedure was used for retrieving the position of isotherm points for simulated temperature fields. Both calculation procedures were written using the Fortran 90 programming language and LabVIEW 2011.

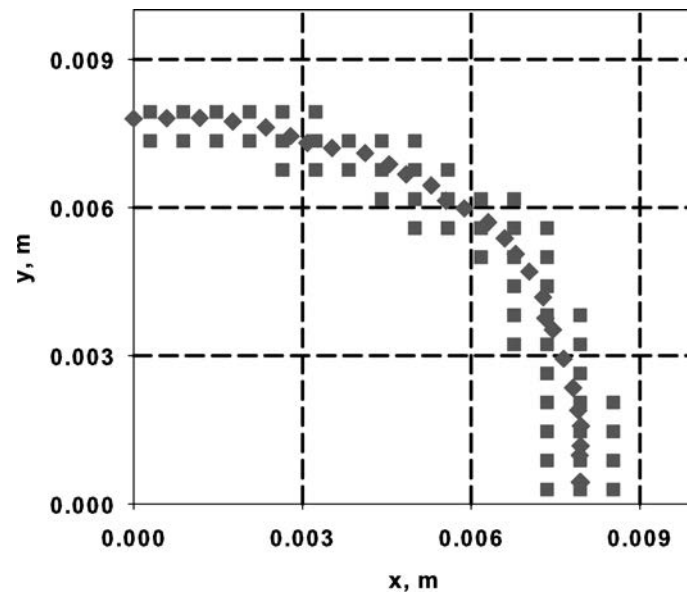


Fig. 6. Evaluated isotherm coordinates (diamond points).

The schematic diagram of the algorithm used for isotherm retrieval procedure for both, measured and calculated data, is shown in Fig. 7. Evaluated positions of isotherms obtained from experiment and simulations are presented in Fig. 8.

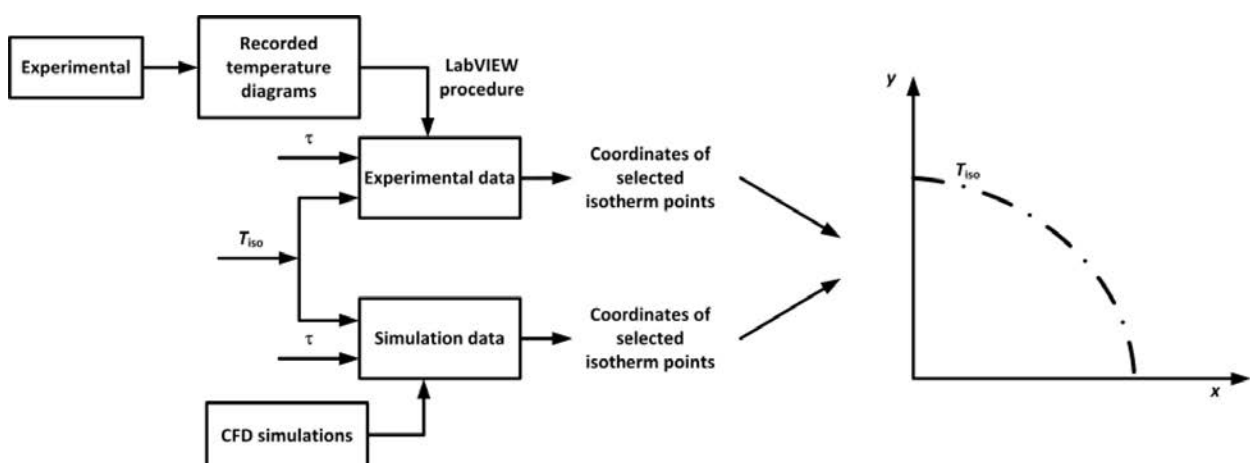


Fig. 7. Schematic diagram of the algorithm used for isotherm retrieval procedure.

Results of calculations show that isotherm positions for all investigated cases were shifted to the right side of experimental results. With increasing simplifications of the numerical model the amount of heat released to the surrounding air decreases, which causes that the isotherm position

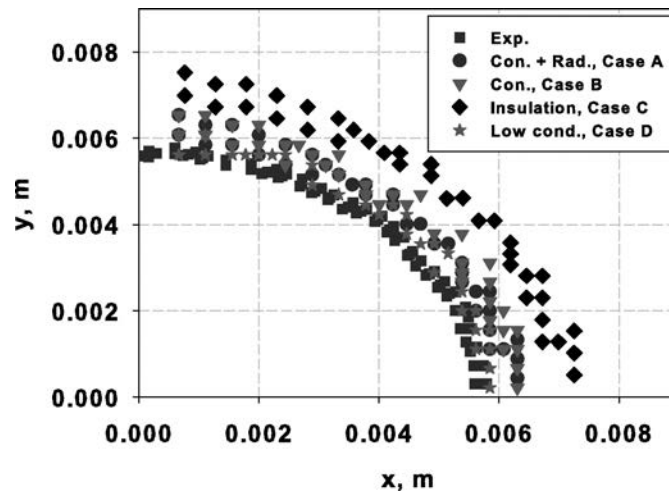


Fig. 8. Evaluated positions of isotherms obtained from experiment and simulations.

is moved farther from the laser emission point. Temperature isotherm in case of the anisotropic (orthotropic) material is of the shape of an ellipse, which can be described by

$$\frac{x^2}{a^2} + \frac{y^2}{b^2} = 1, \quad (14)$$

where x, y are the coordinates of the ellipse points and a, b are ellipse's half axes lengths. In order to estimate the discrepancies between carried out results, the ellipse equation given by Eq. (14) was fitted into the isotherm points for all investigated cases using the Levenberg-Marquardt technique [13]. The obtained lengths of ellipse's half axes are shown in Table 2, whereas the resulting ellipses are depicted in Fig. 9.

Table 2. Calculated ellipse's half axes lengths for all investigated cases.

Ellipse axis	a , mm	b , mm
<i>Exp.</i>	5.70	5.81
<i>Case A</i>	6.18	6.19
<i>Case B</i>	6.31	6.30
<i>Case C</i>	7.12	7.02

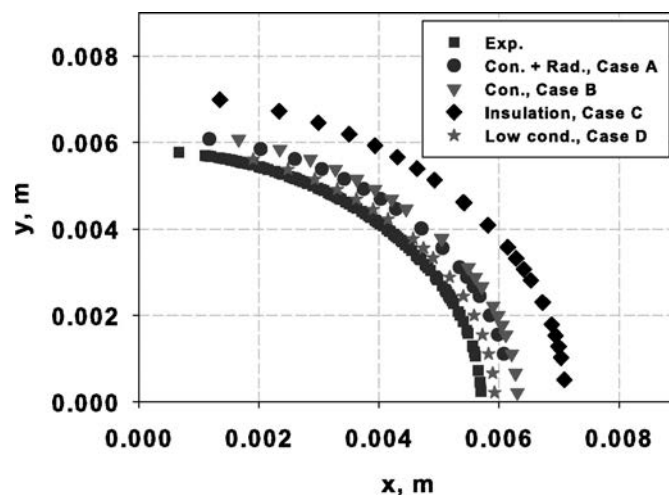


Fig. 9. Isotherms fitted to ellipse equations for all investigated cases.

Interesting situation was observed for *Case A*, where the evaluated numerical results should be comparable with the measured data because both, the radiative and convective heat transfer, were taken into account. The discrepancies could be caused by thermal conductivities specified in the numerical model. Values of thermal conductivities measured by the *in situ* procedure were probably higher than real values of the sample material. It should be kept in mind that each of measurement procedures is laden by an error which influences the level of measured thermal conductivity value. The estimated measuring error for the *in situ* procedure was lower than 5% [4], which means that the exact value of thermal conductivities can change within the range from 4.94 W/mK to 5.46 W/mK. In order to check the impact of thermal conductivity values on the evaluated isotherm position, an additional simulation was performed. *Case D* includes the radiation and convection modeling, but values of thermal conductivities were decreased by 5% of the measured ones. The obtained solution is presented in Fig. 8. It can be seen that this treatment caused shifting of the isotherm position to the left side of experimental data. The exact values of thermal conductivities can be determined by an inverse analysis application, where selected isotherm positions are compared with experimental data by an optimization procedure. The implementation of the inverse analysis for retrieving heat conductivities is the subject of the future model development.

5. CONCLUSIONS

The overall heat losses calculated during the numerical simulation, which included the heat transfer due to the radiation and convection from the measured surface, attained the level of 3 W. Small values of the predicted heat losses justify the assumption made in the developed mathematical model for the *in situ* measurement technique, where the heat dissipation from the measured surface is neglected.

The influence of the radiative and convective heat transfer on a rate of temperature field propagation was investigated for three numerical model configurations. The obtained numerical results show that omitting of heat losses influence the rate of sample cooling and propagation distance of the selected isotherm from the laser emission point. In all investigated cases, positions of the selected isotherm were moved away from experimental data and they were shifted to the right side from the isotherm measured position. The rate of temperature field propagation is affected by values of measured thermal conductivities obtained using the mathematical model employed in the *in situ* measurement technique. Due to the reason that the mathematical model uses the square ratio of half axis of the ellipse for retrieving thermal conductivities, the carried out distance is crucial. Without considering heat losses from the measured surface, the proposed mathematical model slightly overpredicts measured values of thermal conductivities.

The exact effect of the radiation and convection on the level of evaluated thermal conductivities can be investigated by applying the inverse analysis. The inverse model development is the subject of future work, where the CDF model combined with the Levenberg-Marquardt optimization technique will be used for retrieving thermal conductivities of an anisotropic material.

REFERENCES

- [1] W.P. Adamczyk, T. Kruczek, R.A. Bialecki. *6th European Congress on Computational Methods in Applied Sciences and Engineering, ECCOMAS 2012*, 9046, 2012.
- [2] ANSYS, Inc., 2012, available online: <http://www.ansys.com>.
- [3] T. Baba, A. Ono. Improvement of the laser flash method to reduce uncertainty in thermal diffusivity measurements. *Meas. Sci. Technol.*, **12**: 2046, 2001.
- [4] R.A. Bialecki, Z. Buliski. Green's Function in Transient Heat Conduction. In *Encyclopedia of Thermal Stress*, ed. by R.H. Hetnarski, Springer, Berlin 2013 (in press).
- [5] W. Buck, S. Rudtsch. Thermal properties. In *Springer Handbook of Material Measurements*, ed. by H. Czichos, T. Saito, L. Smith, Springer, Heidelberg 2006.
- [6] Y.A. Cengel, A.J. Ghajar. *Heat and mass transfer: fundamentals and applications*. Mc Graw- Hill, 4th edition 2011.

-
- [7] F. Cernuschi, P.G. Bison, A. Figari, S. Marinetti, E. Grinzato. Thermal Diffusivity Measurements by Photothermal and Thermographic Techniques. *Int. J. Thermophys.*, **25**(2): 439–457, 2004.
 - [8] K.D. Cole, A. Haji Sheikh, J.V. Beck, B. Litkouhi. *Heat Conduction Using Green's Function*. CRC Press, Taylor and Francis Group, Boca Raton, 2011.
 - [9] D. Demange P. Beauchene, M. Bejet, R. Casulleras. Simultaneous measurement of thermal diffusivity in the main directions of a material [in French]. *Revue Gen. Thermique*, **36**(10): 755–770, 1997.
 - [10] T. Kruczek, W.P. Adamczyk, R.A. Bialecki. In Situ Measurement of Thermal Diffusivity in Anisotropic Media. *Int. J. of Thermophys.*, **34**(3): 467–485 2013.
 - [11] H.R.B. Orlande, M.N. Ozisik. *Inverse heat transfer: fundamentals and applications*. Taylor and Francis, New York, 2000.
 - [12] W.J. Parker, R.J. Jenkins, C.P. Butler, G.L. Abbott. Method of Determining Thermal Diffusivity, Heat Capacity and Thermal Conductivity. *Journal of Applied Physics*, **32**(9): 1679, 1961. doi: 10.1063/1.1728417.
 - [13] W.H. Press, S.A. Teukolsky, W.T. Vetterling, B.P. Flannery. *Numerical Recipes*. Cambridge, Cambridge University Press, 2007.